1   # Catch me if you can:

2   # Least myelinated white matter develops fastest during early infancy

3

4   Mareike Grotheer[1,2,3*], Mona Rosenke[3], Hua Wu[4], Holly Kular[3], Francesca R. Querdasi[3], Vaidehi Natu[3], Jason D. Yeatman[3,5,6,7], and

5   Kalanit Grill-Spector[3,5]

6   [1] Department of Psychology, Philipps-Universität Marburg, Marburg 35039, Germany.

7   [2] Center for Mind, Brain and Behavior – CMBB, Philipps-Universität Marburg and Justus-Liebig-Universität Giessen, Marburg 35039,

8   Germany.

9   [3] Psychology Department, Stanford University, Stanford, CA 94305, USA.

10 [4] Cognitive and Neurobiological Imaging Center (CNI), Stanford University, Stanford, CA 94305, USA.

11 [5] Wu Tsai Neurosciences Institute, Stanford University, CA 94305, USA.

12 [6] Graduate School of Education, Stanford University, Stanford, CA 94305, USA.

13 [7] Division of Developmental-Behavioral Pediatrics, Stanford University School of Medicine, Stanford, CA 94305, USA.

14

15 *=corresponding author

16

17

18

19

20

21

22

23

24   Development of myelin, a fatty sheath that insulates nerve fibers, is critical for brain

25   function. Myelination during infancy has been studied in postmortem histology, but such

26   data cannot evaluate the developmental trajectory of the white matter bundles of the brain.

27   To address this gap in knowledge, we (i) obtained longitudinal diffusion MRI measures and

28   quantitative MRI measures of T_1, which is sensitive to myelin, from newborns to 6-months-

29   old infants, and (ii) developed an automated fiber quantification method that identifies

30   bundles from dMRI and quantifies their T_1 development in infants. Here we show that both

31   along the length of each bundle and across bundles, T_1 decreases from newborns to 6 months-

32   old's and the rate of T_1 decrease is inversely correlated with T_1 at birth. As lower T_1 indicates

33   more myelin, these data suggest that in early infancy white matter bundles myelinate at

34   different rates such that less mature bundles at birth develop faster to catch-up with the other

35   bundles. We hypothesize that this development reflects experience-dependent myelination,

36   which may promote efficient and coordinated neural communication. These findings open

37   new avenues to measure typical and atypical white matter development in early infancy,

38   which has important implications for early identification of neurodevelopmental disorders.

39

40

41

42

43

44

45

46

2

47   Myelin, the fatty sheath that insulates axons that connect different brain regions is essential

48   for brain function, as it enables rapid and synchronized neural communication across the brain. The

49   formation of myelin, or myelination, is a key hallmark of brain development during infancy, and

50   abnormalities in myelination are linked to a plethora of developmental and cognitive disorders[1]. Classic

51   post-mortem histology reported heterogeneous myelination during infancy[2–5]. However, histological

52   studies compare postmortem brain samples across individuals, often include pathologies, and use

53   observer-dependent methods[6]. Thus, classic histology provides a cross-sectional and qualitative

54   glimpse of myelination. While the heterogenous pattern of development has been replicated[7,8] with

55   modern quantitative MRI (qMRI) [8,16,17], how and at what rate myelin develops in white matter bundles

56   during infancy is unknown.

57   Prior data suggest two hypotheses of myelination in infancy. The starts-first/finishes-first

58   hypothesis proposes that postnatal myelination follows prenatal patterns[2,3,5], predicting that bundles

59   that are more myelinated at birth will develop faster postnatally and finish myelinating earlier

60   (**Supplementary Data 1**). This may allow for most important brain functions to mature faster.

61   Alternatively, the catch-up hypothesis[7,12] suggests that white matter tracts that are less myelinated at

62   birth will develop faster postnatally (**Supplementary Data 1**). This development may be experience-

63   dependent[13–16] and allow for more efficient and coordinated signal transmission across the entire brain.

64   Distinguishing between these hypotheses requires *in-vivo* measurements of the typical,

65   longitudinal developmental of myelin in individual infants and across bundles. While we cannot

66   measure myelin directly *in-vivo,* qMRI enables the measurement of proton relaxation time (T_1 [s]).

67   Notably, 90% of the variance of T_1 in the white matter is driven by myelin[17], whereby higher myelin

68   content results in lower T_1. Thus, we predict that (i) bundles that are more myelinated at birth, will

69   have lower T_1 in newborns than less myelinated bundles, (ii) if myelin increases from 0 to 6 months,

70   then T_1 will decrease from 0 to 6 months, and (iii) if T_1 development follows the starts-first/finishes-

71   first hypothesis T_1 will decrease faster in bundles with lower T_1 at birth, but if T_1 development follows

72   the catch-up hypothesis T_1 will decrease faster in bundles with higher T_1 at birth.

73   To test these predictions, we acquired longitudinal measurements of anatomical MRI,

74   diffusion MRI (dMRI), and qMRI in infants during natural sleep at 3 timepoints: newborn (N=9; age:

75   8-37 days), 3 months (N=10; age: 79-106 days), and 6 months (N=10; age: 167-195 days) of age.

76

Results

New method for automated fiber quantification in infants

79   Evaluating the relationship between myelination at birth and its development across bundles

80   necessitates identifying each individual infant's bundles in their native brain space in a systematic and

81   automated way. A major challenge is that tools developed for adults may not be suitable for infants

82   due to substantial differences in brain size[18] and organization[19]. Thus, we developed a new pipeline for

83   analyzing infant dMRI data and a novel method, baby automated fiber quantification (babyAFQ), for

84   automatically identifying 24 bundles (11 in each hemisphere and 2 between-hemispheres) in each

85   individual infant's brain and timepoint (**Supplementary Data 2-5**). We optimized babyAFQ for

86   infants by: (i) generating waypoints (anatomical ROIs for defining bundles) on a newborn brain

87   template (University of North Carolina (UNC) neonatal template[20]), (ii) decreasing the spatial extent

88   of waypoints compared to adult standard[21] to fit the more compact infant brain, and (iii) adding

89   additional waypoints to better define curved bundles.

90   BabyAFQ successfully identifies 24 bundles in each infant and timepoint (example infant: **Fig.**

91   **1**, all infants: **Supplementary Data 5**), including bundles that have not previously been identified in

92   infants: the posterior arcuate fasciculus[22], vertical occipital fasciculus[22–24], and middle longitudinal

93   fasciculus[25]. The 24 bundles have the expected shape and location in all infants even as their brains

94   grow   from   0   to   6   months.   3D   interactive   visualizations   at   0   months

95   (http://vpnl.stanford.edu/babyAFQ/bb11_mri0_interactive.html),   3   months

96   (http://vpnl.stanford.edu/babyAFQ/bb11_mri3_interactive.html)   and   6   months   of   age

97   (http://vpnl.stanford.edu/babyAFQ/bb11_mri6_interactive.html) show the 3D structure of bundles

98   in an example infant.
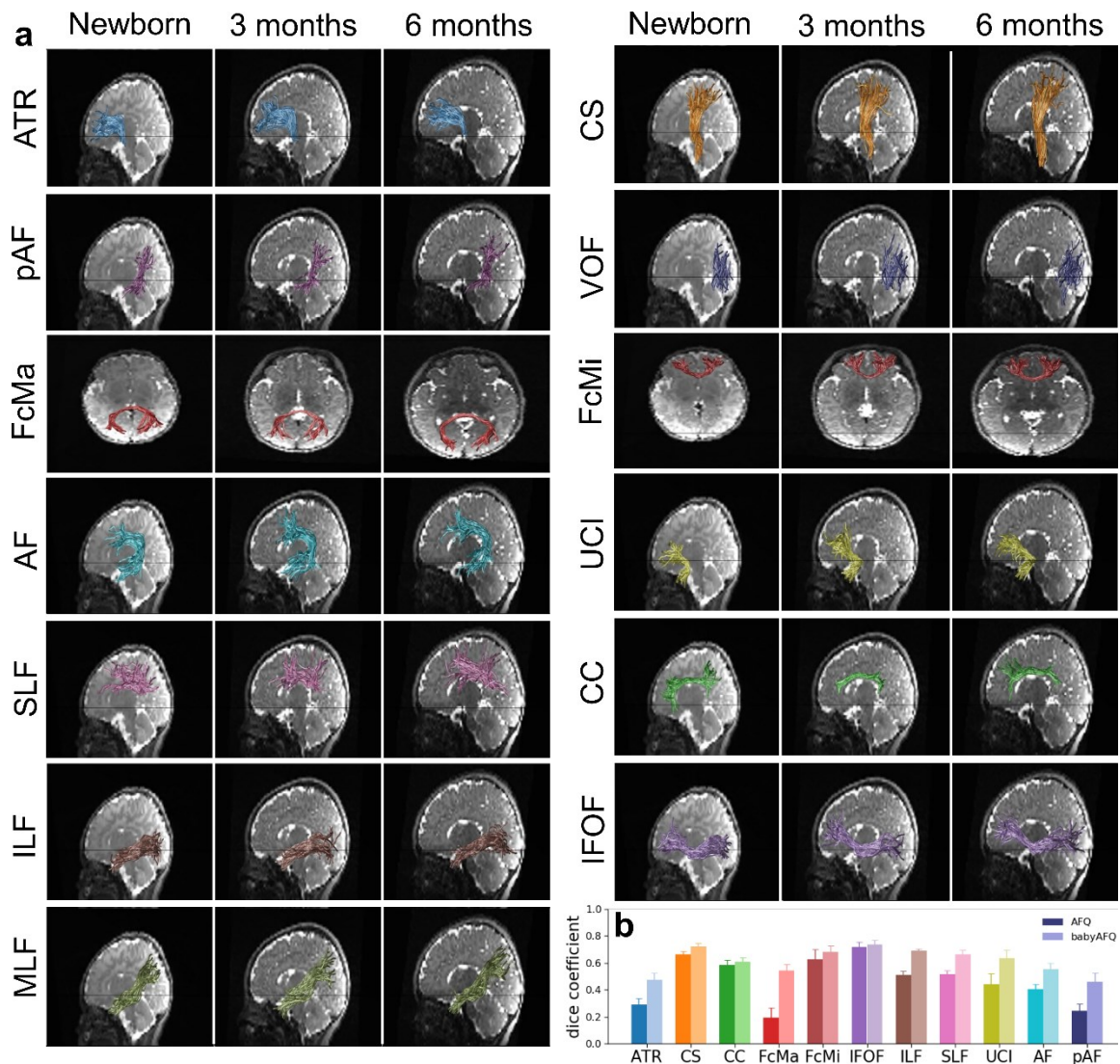
Figure 1. Baby automated fiber quantification (babyAFQ) identifies white matter bundles in individual infant brains across the first 6 months of life. 24 bundles (11 in each hemisphere and 2 cross-hemispheric) were successfully identified in all individuals and ages (**Supplementary Data 3-5**). **a.** All bundles of an individual baby. Each row is a bundle, each column is a timepoint; *left:* newborn, *middle:* 3 months, *right:* 6 months. **b.** Comparison of AFQ and babyAFQ performances in identifying each bundle in newborns relative to manually defined (gold-standard) bundles. The dice coefficient quantifies the overlap between the automatically and manually defined bundles, revealing significantly higher performance for babyAFQ than AFQ. *Abbreviations*: ATR: anterior thalamic radiation, CS: cortico-spinal tract, pAF: posterior arcuate fasciculus, VOF: vertical occipital fasciculus, FcMa: forceps major; FcMi: forceps minor, AF: arcuate fasciculus, UCI: uncinate fasciculus, SLF: superior longitudinal fasciculus, CC: cingulum cingulate, ILF: inferior longitudinal fasciculus, IFOF: inferior frontal occipital fasciculus, MLF: middle longitudinal fasciculus.

99   For quality assurance, we compared babyAFQ and AFQ[26] (developed in adults and used in

100   prior infant studies[27–29]) to manually identified bundles ('gold-standard'). In newborns, bundles

101   identified by babyAFQ substantially overlapped the gold-standard (mean dice coefficient±standard

102   error (SE): 0.61±0.02) and this overlap was significantly higher compared to AFQ (**Fig 1b**; **Fig.**

103   **Supplementary Data 3,5**; 2-way repeated measure analysis of variance (rmANOVA) with AFQ-type

104   and bundle as factors: AFQ-type: $F(1,08)=528.60$, $p<0.0001$, bundle: $F(19,152)=11.31$, $p<0.0001$,

105   AFQ-types x bundle: $F(19,152)=7.13$, $p<0.0001$; additional 3-way rmANOVA on the 11 bilateral

106   bundles, with AFQ-type, bundle, and hemisphere as factors revealed no effects of, or interaction with,

107   hemisphere). Improvements from babyAFQ were also evident at the other timepoints in qualitative

108   evaluations in individual infants. E.g., the Forceps Major was successfully identified by babyAFQ in

109   29/29 brains, but identified by AFQ only in 13/29 brains.

110

T_1 develops faster during early infancy in bundles that are less mature at birth

112   Measurements of mean T_1 of the 24 bundles identified by babyAFQ at 0, 3, and 6 months

113   reveal a substantial decrease in T_1 from 0 to 6 months-olds (**Fig. 2a**). Mean T_1 across bundles±SE

114   [range]: 0 months: 2.2±0.03s [1.86s-2.39s], 3 months: 1.94±0.03s [1.61s-2.18s], 6 months: 1.64s±0.02s

115   [1.40-1.85s]. This is a profound change, as T_1 decreases on average by 0.6s within just 6 months. We

116   modeled T_1 development in each bundle using linear mixed models (LMMs) with age as predictor and

117   a random intercept (estimated T_1 at birth) for each individual. For all bundles, LMMs revealed a

118   negative slope, indicating that T_1 decreases linearly from 0-6 months. Overall, LMMs explained ~90%

119   of the T_1 variance across development (adjusted $Rs^2>0.89$, $ps<0.0001$, for details see **Supplementary**

120   **Table 1**).

121   We next examined if there is a relationship between the rate of T_1 development and T_1 in

122   newborns across bundles. The starts-first/finishes-first hypothesis predicts a positive relationship,

123   whereas the catch-up hypothesis predicts a negative relationship. Results in **Fig 2b** reveal: (i) both

124   mean T_1 in newborns and rate of T_1 development during infancy vary between bundles: e.g., the

125   cortico-spinal tract has lowest newborn T_1 and the Forceps Major has the steepest slope of T_1

126   development, and (ii) there is a significant negative correlation (adjusted R^2=0.35, p=0.001) between

127   the rate of T_1 development (T_1 slope) and mean T_1 measured in newborns. That is, bundles that have

128   higher newborn T_1 (associated with less myelin) have a faster rate of development, which is consistent

129   with the predictions of the catch-up hypothesis.

130   The catch-up hypothesis also predicts that the variability of myelination across bundles will

131   decrease with age, as less mature bundles develop faster. To test this, we compared the standard

132   deviation (SD) of T_1 across bundles for newborns and 6-month-olds. Results indicate that SD of mean

133   T_1 across bundles significantly decreases (two-sample t-test: t(17)=7.49, p<0.0001) from newborns

134   (0.14s±0.0009s, SD±SE) to 6-months-olds (0.11s±0.0007s), consistent with this prediction.
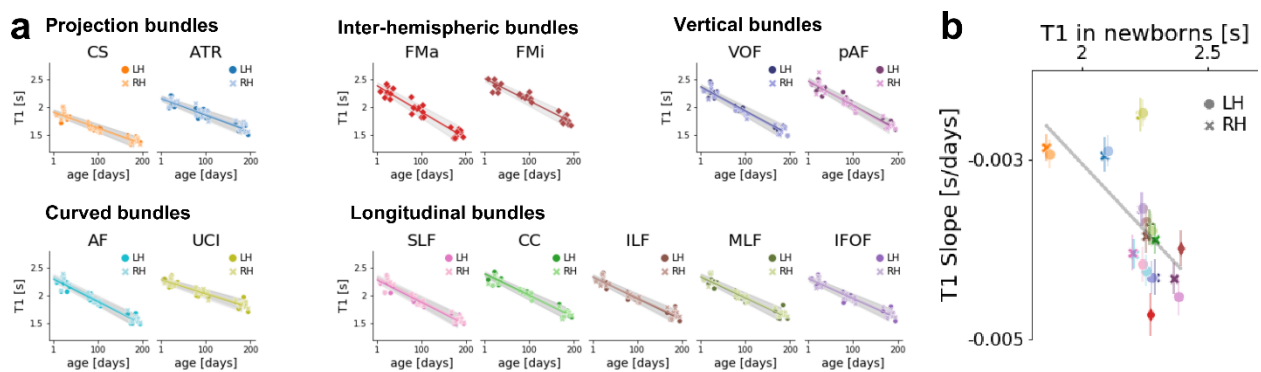
Figure 2. T_1 of white matter bundles linearly decreases from birth to 6 months of age. a. Mean T_1 of each bundle as a function of age in days. Each point is a participant; markers indicate hemisphere; lines indicate LMM prediction; lines for both hemispheres fall on top of each other; gray shaded regions indicate 95% confidence interval. **b.** Bundles' development rate (T1 slope) is significantly and negatively correlated with bundles' T1 in newborns, consistent with the catch-up hypothesis. *Error bars*: SE. *Abbreviations:* LH: left hemisphere, RH: right hemisphere

135

T_1 varies across the length of a given bundle in early infancy

137   Our data show that bundles that are less mature in newborns develop faster than those that

138   are more mature in newborns. As white matter bundles are large structures that connect cortical

139   regions across brain lobes, an important question is whether T_1 development varies across the length

140   of bundles.

141   Analysis of T_1 along bundles (**Fig 3**) using babyAFQ reveals three main findings: (i) Some

142   bundles illustrate substantial variations in T_1 (e.g., cortico-spinal tract), while others exhibit only

143   modest variations (e.g., vertical occipital fasciculus). (ii) Consistent with the prior analyses, across the

144   lengths of bundles, T_1 systematically decreases from newborns (**Fig 3-dotted line**) to 3-month-olds

145   (**Fig 3-dashed line**) to 6-months-olds (**Fig 3-solid line**). (iii) The fluctuation in T_1 among nearby

146   points along bundles decreases from newborns to 6-month-olds. That is, the variability in T_1 between

147   nonoverlapping, nearby positions along the length of each bundle (sum of squared difference (SSD)

148   of T_1 values between positions that are 10 nodes apart) significantly decreased (two-sample t-test:

149    $t(17)=3.29$ $p=0.004$) from $0.08s\pm0.001s$ (mean SSD across bundles$\pm$SE) in newborns to

150    $0.07s\pm0.0007s$ in 6-months-olds.
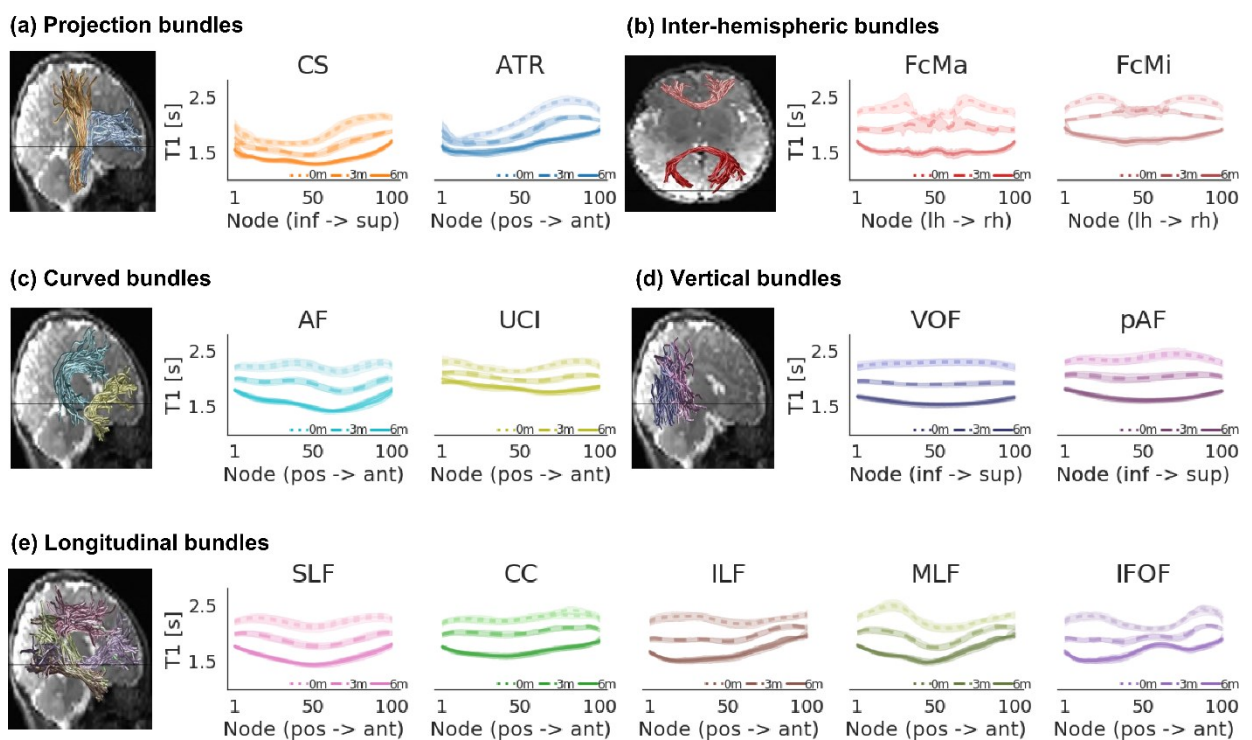
151

**Figure 3. Development of T_1 along each bundle.** Mean T_1 across infants is displayed in both hemispheres (lines for the two hemispheres fall on top of each other) along the length of each bundle in newborns (0m, dotted line), 3-months-olds (3m, dashed line), and 6-months-olds (6m, solid line). Shaded regions: 95% confidence intervals. Left panels show the bundles in a representative newborn.

152

153

154

8

Segments of infants' bundles with less mature T_1 at birth develop at a faster rate

155

156   We next determined the rate of T_1 development across the length of each bundle, by using

157   LMMs to relate T_1 to age at 100 equidistant locations (nodes) (one LMM per node and bundle; random

158   intercepts for individuals). Examination of the rate of T_1 development (**Fig 4-dashed lines**) relative

159   to the measured T_1 in newborns (**Fig 4-solid lines**, left y-axis), reveals that (i) even as the slopes are

160   negative throughout, the rate of T_1 decrease varies across the length of the bundles and (ii) segments

161   of bundles that are less mature in newborns (higher T_1) have a steeper rate of T_1 decrease (more

162   negative slopes) than segments than are more mature in newborns. E.g., the superior aspect of the

163   cortico-spinal tract has higher T_1 in newborns than its inferior aspect, and correspondingly, a more

164   negative slope.
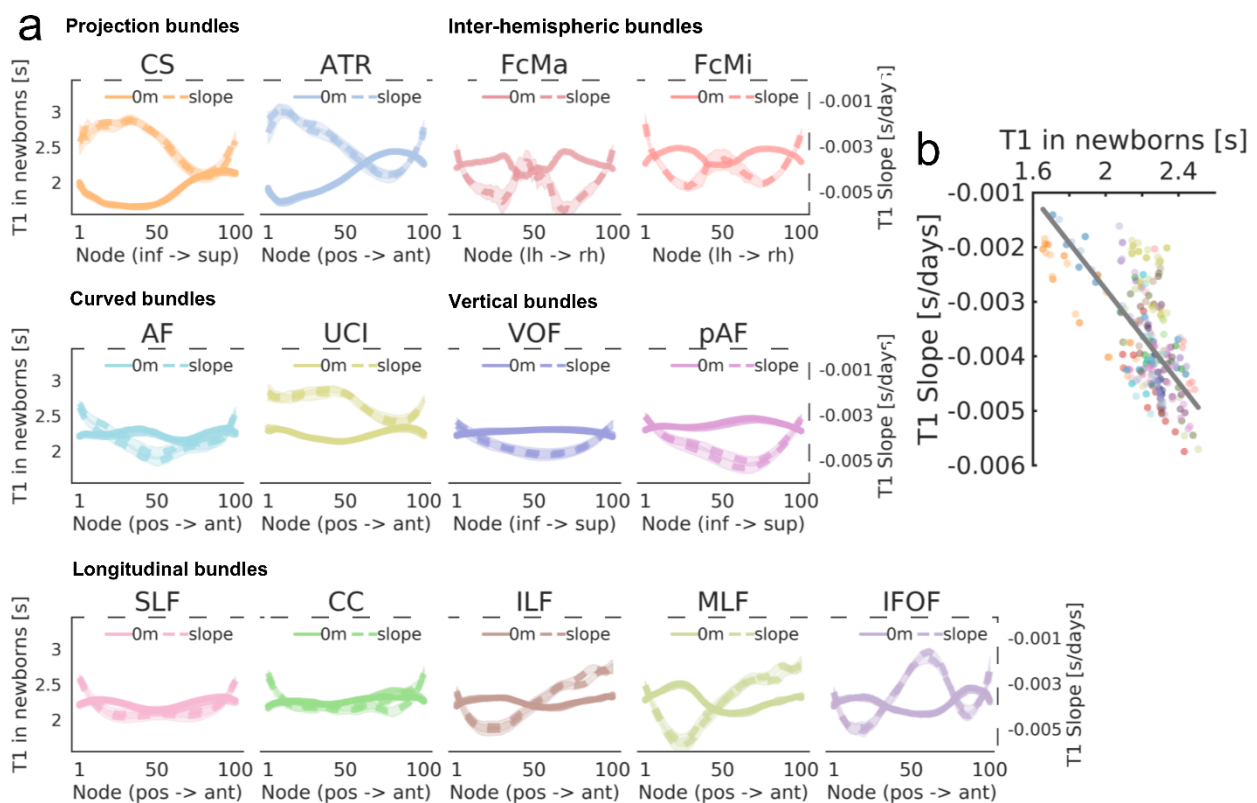
Figure 4. Negative relationship between T_1 development rate and T_1 in newborns along the length of each bundle. a. Each panel jointly shows measured T_1 in newborns (left y axis, solid line) and the slope of T_1 development (right y axis, dashed line) at each node along the bundle. Faster development (more negative slope) corresponds to lower values of dashed lines. Higher T_1 in newborns correspond to higher values in solid lines. Lines from both hemispheres are presented separately but fall on top of each other. **b.** LMM relating slope of T_1 development and T_1 in newborns at independent locations along the length of each bundle reveals a significant negative relationship (gray line) as predicted by the catch-up hypothesis.

9

165   We quantified the relationship between the slope of T_1 development and the measured T_1 in

166   newborns at nonoverlapping positions (every 10th node) along all bundles (LMM relating T_1 slope to

167   measured T_1 in newborns; random intercepts for each bundle). This analysis reveals a significant

168   negative relationship (**Fig 4b**, adjusted $R^2=0.64$, $p<0.0001$) between T_1 development rate and

169   measured T_1 in newborns along the length of these bundles. Results suggest that segments of bundles

170   that are more mature at birth develop slower than segments that are less mature at birth as predicted

171   by the catch-up hypothesis.

172

173   **Discussion**

174   By combining a novel approach for white matter bundle delineation in individual infant brains

175   (babyAFQ) with new longitudinal measures of quantitative T_1, we find a substantial decrease in T_1

176   across all investigated bundles during early infancy. Notably, both within and across bundles, the rate

177   of T_1 development shows a negative relationship with the initial T_1 in newborns. As T_1 is inversely

178   correlated with myelination, this suggests that bundles and their segments that are less myelinated in

179   newborns develop faster, consistent with the predictions of the catch-up hypothesis of infant myelin

180   development.

181   The finding that less mature white matter at birth myelinates faster during infancy is important

182   for several reasons. First, our data not only provides empirical evidence against the classic view that

183   white matter develops in a strictly hierarchically manner from early sensory to higher-level cognitive

184   regions[2,3], but it also offers a new parsimonious explanation for the heterogenous nature of white

185   matter development in infancy. As myelination is experience-dependent[13–16], our data suggests that the

186   new postnatal environment and experiences may produce a flurry of myelination during the first 6

187   months of life, overtaking the earlier prenatal gradients. For example, projection bundles associated

188   with movement receive input already *in utero* and develop slowly after birth, while bundles that connect

189   sensory or higher order regions may only begin to receive input after birth and develop quickly

190   thereafter. Due to this, myelination may also be fine-tuned based on each individual infant's

191 experience. Second, we further hypothesize that the resulting negative relationship between

192 myelination at birth and the rate of myelin development is functionally relevant. Due to this, some

193 level of myelin will arise in all bundles during early infancy, which may enable more coordinated and

194 effective communication across the brain. Third, our data help interpret developmental trajectories of

195 diffusion metrics in infants[11,12,30,31]. Specifically, diffusion metrics that develop similarly to T_1 may be

196 more closely related to myelination than metrics with a different developmental trajectory. Thus,

197 future studies combining multiple quantitative and diffusion MRI metrics[32–34] may disentangle multiple

198 aspects of white matter microstructural development including not only myelination but also fiber

199 organization, packing, and diameter.

200 Crucially, due to the quantitative nature of T_1[7–9], we can compare our measurements to other

201 populations. E.g., in our newborn bundles, T_1 varies between 1.86s-2.39s, which is lower than T_1 of

202 2.75s-3.5s observed in the white matter of preterm infants[35]. This observation suggests some

203 myelination in all evaluated bundles in full-term newborns, which contrasts with classic histological

204 studies[2–5] that reported perinatal myelination in only a few white matter bundles. As classic studies

205 used qualitative visual inspection of myelin stains, our data underscore the utility of quantitative T_1

206 measurements. Our measurements also reveal that T_1 in bundles of 6-months-olds ranges between

207 1.40s-1.85s, which is higher than the 0.8s-1.2s rage reported in adults[36,37], suggesting that none of the

208 investigated bundles are fully myelinated by 6 months of age. Future longitudinal investigations over

209 a longer period are necessary to determine when these bundles reach adult-like myelination. Finally,

210 we find that mean T_1 across bundles decreases on average by 0.6s within just 6 months, which is 10

211 times larger than the decrease of ~0.05s observed between 8 and 18 years of age[36], which highlights

212 the profound changes occurring in early infancy.

213 Our study has important societal implications. First, T_1 values are quantitative and have units

214 that can be numerically compared across scanners, populations, and individuals[9]. Thus, our

215 measurements in typically-developing infants provide a key foundation for large-scale studies of infant

216 brain development in typical[38,39] and clinical populations such as preterm infants[40], infants with

217   cerebral palsy[41], or fetal alcohol spectrum disorders[42]. Second, our methodology is translatable to

218   clinical settings as it is performed during natural sleep. Third, we developed an automated pipeline

219   that simultaneously provides high throughput and high precision in individual infants. This level of

220   precision may enable early identification of developmental impairments in at-risk infants, which in

221   turn may improve the efficacy of interventions[43].

222   In conclusion, we find that during early infancy less mature white matter at birth develops

223   faster than more mature white matter, equalizing myelination across white matter bundles. This

224   finding offers a new parsimonious explanation of white matter development in early infancy. We

225   hypothesize that this pattern of myelination in infancy is driven by experience and ensures that a

226   minimal amount of myelin becomes quickly available throughout the brain, which may serve to

227   promote efficient and coordinated communication across the brain.

228

229   **Methods**

230   **Participants**

231   16 full-term and healthy infants (7 female) were recruited to participate in this study. Three

232   infants provided no usable data because they could not stay asleep once the MRI sequences started

233   and hence, we report data from 13 infants (6 female) across three timepoints: newborn (N=9; age: 8-

234   37 days), 3 months (N=10; age: 79-106 days), and 6 months (N=10; age: 167-195 days). Two

235   participants were re-invited to complete scans for their 6-months session that could not be completed

236   during the first try. Both rescans were performed within 7 days and participants were still within age

237   range for the 6-months timepoint. The participant population was racially and ethnically diverse

238   reflecting the population of the Bay Area, including two Hispanic, nine Caucasian, two Asian, and

239   three multiracial participants. Six out of the 13 infants participated in MRI in all three timepoints (0,

240   3, 6 months). Due to the Covid-19 pandemic and restricted research guidelines, data acquisition was

241   halted. Consequently, the remaining infants participated in either 1 or 2 sessions.

242   Expectant mothers and their infants in our study were recruited from the San Francisco Bay

243   Area using social media platforms. We performed a two-step screening process for expectant mothers.

244   First, mothers were screened over the phone for eligibility based on exclusionary criteria designed to

245   recruit a sample of typically developing infants and second, eligible expectant mothers were screened

246   once again after giving birth. Exclusionary criteria for expectant mothers were as follows: recreational

247   drug use during pregnancy, significant alcohol use during pregnancy (more than 3 instances of alcohol

248   consumption per trimester; more than 1 drink per occasion), lifetime diagnosis of autism spectrum

249   disorder or a disorder involving psychosis or mania, taking prescription medications for any of these

250   disorders during pregnancy, written and spoken English ability insufficient to participate in the study,

251   and learning differences that would preclude participation in the study. Exclusionary criteria for infants

252   were: preterm birth (<37 gestational weeks), low birthweight (<5 lbs 8 oz), small height (<18 inches),

253   any congenital, genetic, and neurological disorders, visual problems, complications during birth that

254   involved the infant (e.g., NICU stay), history of head trauma, and contraindications for MRI (e.g.,

255   metal implants).

256

Data Acquisition Procedure

258   Data collection procedure was developed in a recent study[44]. All included participants

259   completed the multiple scanning protocols needed to obtain anatomical MRI, qMRI, and dMRI data.

260   Data were acquired at two identical 3T GE Discovery MR750 Scanners (GE Healthcare) and Nova

261   32-channel head coils (Nova Medical) located at Stanford University: (i) Center for Cognitive and

262   Neurobiological Imaging (CNI) and (ii) Lucas Imaging Center. As infants have low weight, all imaging

263   was done with first level SAR to ensure their safety. Study protocols for these scans were approved

264   by the Stanford University Internal Review Board on Human Subjects Research.

265   Scanning sessions were scheduled in the evenings close in time to the infants' typical bedtime.

266   Each session lasted between 2.5 − 5 hours including time to prepare the infant and waiting time for

267   them to fall asleep. Upon arrival, caregivers provided written, informed consent for themselves and

268   their infant to participate in the study. Before entering the MRI suite, both caregiver and infant were

269   checked to ensure that they were metal-free and caregivers changed the infants into MR safe cotton

270   onesies and footed pants provided by the researchers. The infant was swaddled with a blanket with

271   their hands to their sides to avoid their hands creating a loop. During sessions involving newborn

272   infants, an MR safe plastic immobilizer (MedVac, www.supertechx-ray.com) was used to stabilize the

273   infant and their head position. Once the infant was ready for scanning, the caregiver and infant entered

274   the MR suite. The caregiver was instructed to follow their child's typical sleep routine. As the infant

275   was falling asleep, researchers inserted soft wax earplugs into the infant's ears. Once the infant was

276   asleep, the caregiver was instructed to gently place the infant on a makeshift cradle on the scanner

277   bed, created by weighted bags placed at the edges of the bed to prevent any side-to-side movement.

278   Finally, to lower sound transmission, MRI compatible neonatal Noise Attenuators

279   (https://newborncare.natus.com/products-services/newborn-care-products/nursery-

280   essentials/minimuffs-neonatal-noise-attenuators) were placed on the infant's ears and additional pads

281   were also placed around the infant's head to stabilize head motion.

282   An experimenter stayed inside the MR suite with the infant during the entire scan. For

283   additional monitoring of the infant's safety and lack of motion, an infrared camera was affixed to the

284   head coil and positioned for viewing the infant's face in the scanner. The researcher operating the

285   scanner monitored the infant via the camera feed, which allowed for the scan to be stopped

286   immediately if the infant showed signs of waking or distress. This setup also allowed tracking the

287   infant's motion; scans were stopped and repeated if there was excessive head motion. To ensure scan

288   data quality, in addition to real-time monitoring of the infant's motion via an infrared camera, MR

289   brain image quality was also assessed immediately after acquisition of each sequence and repeated if

290   necessary.

291

292

293

294 **Data Acquisition Parameters and Preprocessing**

295 <u>Anatomical MRI:</u> T2-weighted images were acquired and used for tissue segmentations. T2-

296 weighed image acquisition parameters: TE=124 ms; TR = 3650ms; echo train length = 120; voxel size

297 = $0.8mm^3$; FOV=20.5cm; Scan time: 4 min and 5 sec.

298 We generated gray/white matter tissue segmentations of all infants and time-points and used

299 them to optimize tractography (anatomically constrained tractography, ACT[45]). The T2-weighted

300 anatomy, and a synthetic T1-weighted whole brain image generated from the SPGRs and IR-EPI

301 scans using mrQ software (https://github.com/mezera/mrQ) were aligned and used for

302 segmentations. Multiple steps were applied to generate accurate segmentations of each infant's brain

303 at each timepoint[44]. (1) An initial segmentation of gray and white matter was generated from the T1-

304 weighted brain volume using infant FreeSurfer's automatic segmentation code that expects T1-

305 weighted input (infant-recon-all; https://surfer.nmr.mgh.harvard.edu/fswiki/infantFS[46]). (2) The T2-

306 weighted anatomical images, which have a better contrast between gray and white matter in infants,

307 were used in an independent brain extraction toolbox (Brain Extraction and Analysis Toolbox,

308 iBEAT, v:2.0 cloud processing, https://ibeat.wildapricot.org/[47–49]) to generate another, more accurate,

309 white and gray matter segmentation. (3) The iBEAT segmentation was manually corrected to fix

310 segmentation errors (such as holes and handles) using ITK-SNAP (http://www.itksnap.org/). (4) The

311 iBEAT segmentation was then reinstalled to FreeSurfer and the resulting segmentation in typical

312 FreeSurfer format was used to optimize tractography.

313

314 <u>Quantitative MRI:</u> Spoiled-gradient echo images (SPGRs) were used together with the

315 Inversion-recovery EPI (IR-EPI) sequence to estimate T_1 relaxation time at each voxel and to generate

316 whole-brain synthetic T_1-weighted images. We acquired 4 SPGRs whole brain images with different

317 flip angles: α = 4°, 10°, 15°, 20°; TE=3ms; TR =14ms; voxel size=$1mm^3$; number of slices=120;

318 FOV=22.4cm; Scan time: 4 times ~5 minutes. We also acquired multiple inversion times (TI) in the

15

319   IR-EPI using a slice-shuffling technique[50]: 20 TIs with the first TI=50ms and TI interval=150ms as

320   well as a second IR-EPI with reverse phase encoding direction. Other acquisition parameters were:

321   voxel size=2mm^3; number of slices=60; FOV=20cm; in-plane/through-plane acceleration=1/3; Scan

322   time=two times 1:45 min.

323   IR-EPI data were used to estimate T_1 relaxation time at each voxel. First, as part of the

324   preprocessing, we performed susceptibility-induced distortion correction on the IR-EPI images using

325   FSL's top-up and the IR-EPI acquisition with reverse phase encoding direction. We then used the

326   distortion corrected images to fit the T_1 relaxation signal model using a multi-dimensional Levenberg-

327   Marquardt algorithm[51]. The signal equation of T_1 relaxation of an inversion-recovery sequence is an

328   exponential decay:

329      $$S(t) = a(1 - be^{-t/T1}),$$

330   where t is the inversion time, a is proportional to the initial magnetization of the voxel, b is

331   the effective inversion coefficient of the voxel (for perfect inversion b=2). To work with magnitude

332   images, we took the absolute value of the above signal equation and used it as the fitting model. The

333   output of the algorithm is the estimated T_1 in each voxel.

334

335   <u>Diffusion MRI:</u> We obtained dMRI data with the following parameters: multi-shell, #diffusion

336   directions/b-value = 9/0, 30/700, 64/2000; TE = 75.7 ms; TR=2800ms; voxel size = 2mm^3; number

337   of slices=60; FOV=20cm; in-plane/through-plane acceleration = 1/3; Scan time: 5:08 min. We also

338   acquired a short dMRI scan with reverse phase encoding direction and only 6 b=0 images (scan time

339   0:20 min).

340   dMRI preprocessing was performed in accordance with recent work from the developing

341   human connectome project[52,53], using a combination of tools from MRtrix3[54,55]

342   (github.com/MRtrix3/mrtrix3) and mrDiffusion (http://github.com/vistalab/vistasoft). We (i)

343   denoised the data using a principal component analysis[56], (ii) used FSL's top-up tool

344 (https://fsl.fmrib.ox.ac.uk/) and one image collected in the opposite phase-encoding direction to

345 correct for susceptibility-induced distortions, (iii) used FSL's eddy to perform eddy current and motion

346 correction, whereby motion correction included outlier slice detection and replacement[57] and (iv)

347 performed bias correction using ANTs[58]. The preprocessed dMRI images were registered to the

348 whole-brain T2-weighted anatomy using whole-brain rigid-body registration and alignment quality was

349 checked for all images. dMRI quality assurance was also performed. Across all acquisitions, less than

350 $5\% \pm 0.72\%$ of dMRI images were identified as outliers by FSL's eddy tool. We found no significant

351 effect of age across the outliers (no main effect of age: $F(2,26)=1.97$, $p=0.16$, newborn: $1.07+0.88\%$;

352 3 months: $0.4+0.40\%$; 6 months: $0.67+0.85\%$), suggesting that the developmental data was well

353 controlled across all time-points.

354   Next, voxel-wise fiber orientation distributions (FODs) were calculated using constrained

355 spherical deconvolution (CSD) in MRtrix3[54] (**Supplementary Data 2**). We used the Dhollander

356 algorithm[59] to estimate the three-tissue response function, and we lowered the FA threshold to 0.1 to

357 account for the generally larger FA in infant brains. We computed FODs with multi-shell multi-tissue

358 CSD[60] separately for the white matter and the CSF. As in previous work[52], the gray matter was not

359 modeled separately, as white and gray matter do not have sufficiently distinct b-value dependencies to

360 allow for a clean separation of the signals. Finally, we performed multi-tissue informed log-domain

361 intensity normalization.

362   We used MRtrix3[54] to generate a whole brain white matter connectome for each subject.

363 Tractography was optimized using the tissue segmentation from anatomical MRI (anatomically-

364 constrained tractography, ACT[45]). We argue that this approach is particularly useful for infant data, as

365 gray and white matter cannot be separated in the FODs. For each connectome, we used probabilistic

366 fiber tracking with the following parameters: algorithm: IFOD1, step size: 0.2 mm, minimum length:

367 4 mm, maximum length: 200 mm, FOD amplitude stopping criterion: 0.05, maximum angle: 15°.

368 Seeds for tractography were randomly placed within the gray/white matter interface (from anatomical

17

369 tissue segmentation), which enabled us to ensure that tracts reach the gray matter. Each connectome

370 consisted of 2 million streamlines.

371

Bundle delineation with baby automated fiber quantification (babyAFQ)

373 Here we developed a new toolbox (babyAFQ) for the identification of white matter bundles

374 in individual infants, that is openly available as a novel component of AFQ[26]

375 (https://github.com/yeatmanlab/AFQ/tree/master/babyAFQ). BabyAFQ identifies the following

376 bundles (**Fig. 1**): anterior thalamic radiation (ATR), cortico-spinal tract (CS), posterior arcuate

377 fasciculus (pAF), vertical occipital fasciculus (VOF), forceps major (FcMa), forceps minor (FcMi),

378 arcuate fasciculus (AF), uncinate fasciculus (UCI), superior longitudinal fasciculus (SLF), cingulum

379 cingulate (CC), inferior longitudinal fasciculus (ILF), inferior frontal occipital fasciculus (IFOF) and

380 the middle longitudinal fasciculus (MLF).

381 BabyAFQ uses anatomical ROIs as waypoints for each bundle, that is, a given tract is

382 considered a candidate for belonging to a bundle if it passes through all waypoints. The waypoint

383 ROIs were adjusted from those commonly used in adults[21] to better match the head size and white

384 matter organization of infants (**Supplementary Data 3**). Specifically, we: (i) spatially restricted some

385 of the waypoint ROIs, (ii) introduced a third waypoint for curvy bundles, (iii) changed the waypoint

386 ROIs for the VOF from surface ROIs to volumetric ROIs (**Supplementary Data 4**), as cortical

387 surface reconstructions in infants are challenging to date and (iv) added way-point ROIs for the

388 identification of the MLF, which was not included in prior AFQ versions. Critically, these waypoints

389 were defined in a neonate infant template brain (UNC Neonatal template[20]) and are transformed from

390 this template space to individual infant brain space before bundle delineation in each infant's brain.

391 The use of an infant template brain is critical as commonly used adult templates, such as the MNI

392 brain, are substantially larger and difficult to align to infant data. In cases where a given tract is a

393 candidate for multiple bundles, a probabilistic atlas, which is also transformed from infant template

394 space to individual infant brain space, is used to determine which bundle is the better match for the

18

395   tract. Bundles are then cleaned by removing tracts that exceed a gaussian distance of 4 from the core

396   of the bundle.

397   Critically, babyAFQ was designed to seamlessly integrate with AFQ, so that additional tools

398   for plotting, tract profile evaluation and statistical analysis can be applied after bundle delineation.

399

400   **BabyAFQ quality assurance**

401   In order to evaluate the quality of the bundle delineation in babyAFQ, we compared the

402   identified bundles to manually delineated "gold-standard" bundles. Manual bundle delineation was

403   performed for the newborns in DSI Studio (http://dsi-studio.labsolver.org/) by 2 anatomical experts

404   who were blinded to the results of babyAFQ. As a benchmark, we also delineated bundles with AFQ

405   developed using adult data and compared these bundles to the manual bundles. For both babyAFQ

406   and AFQ we quantified the spatial overlap between the automatically identified bundles and the

407   manual bundles using the dice coefficient[61] (DC): $DC = \frac{2|A \cap B|}{|A|+|B|}$, where $|A|$ are voxels of

408   automatically-identified bundles, $|B|$ are voxels of the manual bundles, and $|A \cap B|$ is the

409   intersection between these two sets of voxels (**Fig. 1b**). We compared dice coefficients between

410   babyAFQ and AFQ in two rmANOVAs. First, a 2-way rmANOVA with AFQ-type and bundle as

411   factors allowed us to evaluate the effect of AFQ type across all bundles. Second, a 3-way rmANOVA

412   with AFQ-type, bundle and hemisphere as factors, that only included bilateral bundles, enabled us to

413   test for hemispheric differences. Finally, we also used the dice coefficients to test if tracts identified

414   to be part of the VOF are similar across methods – i.e., using volumetric way-point ROIs vs. surface

415   ROIs (**Supplementary Data 4**).

416   In addition to the quantitative evaluation, we examined all bundles delineated using babyAFQ

417   and AFQ qualitatively at all time-points (**Supplementary Data 5**), by evaluating how well they match

418   the typical spatial extent and trajectory. We also provide an interactive 3D visualization of an example

419   infant's bundles (created with pyAFQ[62]).

Modeling T_1 developement

420

421   After identifying all bundles with babyAFQ, we modeled their T_1 development using mixed

422 linear models (LMMs). First, we modeled mean T_1 development within each bundle using LMMs with

423 age as predictor and a random intercept (estimated T1 at birth) for each individual (**Fig 2a**). We used

424 model comparison (likelihood ratio tests) to determine that LMMs allowing different slopes for each

425 individual do not better explain the data compared to LMMs using a single slope across individuals.

426 To distinguish between the starts-first/finishes-first hypothesis and the catch-up hypothesis, we then

427 related the developmental slopes from the LMMs and the T_1 in newborns across bundles (**Fig 2b**).

428 Finally, we compared the standard deviation in T_1 across bundles between newborns and 6 months-

429 olds with 2-sample t-tests.

430   Next, we evaluated the development of T_1 across the length of each bundle. For this, we

431 divided each bundle into 100 equidistant locations (nodes) and visually inspected T_1 at each time-point

432 across these nodes (**Fig 3**). We observed that the fluctuation in T_1 among nearby nodes decreased

433 with age, and quantified this observation by comparing the sum of squared difference (SSD) between

434 positions that are 10 nodes apart in the newborns and the 6-months-olds with 2-sample t-tests.

435   We then determined the rate of T_1 development across the length of each bundle by fitting

436 LMMs that relate T_1 to age at each node (one LMM per bundle; random intercepts for each individual

437 as above, **Fig 4a**). Finally, we evaluated the relationship between the slope of T_1 development and the

438 measured T_1 in newborns at nonoverlapping positions (every 10th node) along all bundles (LMM

439 relating T1 slope to measured T_1 in newborns, random intercepts for each bundle, **Fig 4b**). We used

440 model comparison (likelihood ratio test) to determine that a LMM allowing different slopes for each

441 bundle does not better explain the data compared to this LMM.

442

443

444

445   **Data and code availability**

446   The data were analyzed using open source software, including mrDiffusion and MRtrix3[54]. We

447   developed a new toolbox for automatic fiber quantification in individual infants (babyAFQ) and make

448   it openly available (https://github.com/yeatmanlab/AFQ/tree/babyAFQ/babyAFQ). Code for

449   reproducing all figures is made available in GitHub as well (https://github.com/VPNL/CatchUp).

450   The data generated in this study will be made available by the corresponding author upon reasonable

451   request.

452

453   **Acknowledgements**

461

462   **Author contribution**

463   MR, HK, and FRQ collected the data. MR, VN, HK and FRQ generated gray/white matter

464   segmentations and T_1 maps. HW developed scanning sequences. MG and JDY developed babyAFQ

465   and data analysis pipeline. MG, JDY and KGS analyzed data. MG and KGS wrote initial draft of the

466   manuscript. All authors edited and improved the initial draft.

467

468

Competing Interests

469

470   The authors declare no competing interests.

471

References:

472

473   1.   Fields, R. D. White matter in learning, cognition and psychiatric disorders. *Trends in*
474   *Neurosciences* **31**, 361–370 (2008).

475   2.   Flechsig, P. . Anatomie des menschlichen Gehirns und Rückenmarks aus myelogenetischer
476   Grundlage. *JAMA J. Am. Med. Assoc.* **76**, 676 (1921).

477   3.   Yakovlev, P. I. & Lecours, A.-R. The myelogenetic cycles of regional maturation of the brain.
478   in *Regional Development of Brain in Early Life* 3–70 (1967).

479   4.   Kinney, H. C., Brody, B. A., Kloman, A. S. & Gilles, F. H. Sequence of central nervous
480   system myelination in human infancy: II. Patterns of myelination in autopsied infants. *J.*
481   *Neuropathol. Exp. Neurol.* **47**, 217–234 (1988).

482   5.   Gilles, F. H., Shankle, W. & Dooling, E. C. MYELINATED TRACTS: GROWTH
483   PATTERNS. in *The Developing Human Brain* 117–183 (Elsevier, 1983). doi:10.1016/b978-0-
484   7236-7017-9.50018-1

485   6.   Schleicher, A., Amunts, K., Geyer, S., Morosan, P. & Zilles, K. Observer-independent
486   method for microstructural parcellation of cerebral cortex: A quantitative approach to
487   cytoarchitectonics. *Neuroimage* **9**, 165–177 (1999).

488   7.   Deoni, S. C. L. *et al.* Mapping infant brain myelination with magnetic resonance imaging. *J.*
489   *Neurosci.* **31**, 784–791 (2011).

490   8.   Deoni, S. C. L., Dean, D. C., O'Muircheartaigh, J., Dirks, H. & Jerskey, B. A. Investigating
491   white matter development in infancy and early childhood using myelin water faction and
492   relaxation time mapping. *Neuroimage* **63**, 1038–1053 (2012).

493   9.   Mezer, A. *et al.* Quantifying the local tissue volume and composition in individual brains with
494   magnetic resonance imaging. *Nat. Med.* **19**, 1667–1672 (2013).

495   10.   Weiskopf, N., Mohammadi, S., Lutti, A. & Callaghan, M. F. Advances in MRI-based
496   computational neuroanatomy: From morphometry to in-vivo histology. *Curr. Opin. Neurol.* **28**,
497   313–322 (2015).

498   11.   Qiu, A., Mori, S. & Miller, M. I. Diffusion tensor imaging for understanding brain
499   development in early life. *Annu. Rev. Psychol.* **66**, 853–876 (2015).

500   12.   Dubois, J. *et al.* Exploring the Early Organization and Maturation of Linguistic Pathways in
501   the Human Infant Brain. *Cereb. Cortex* **26**, 2283–2298 (2016).

502   13.   Zatorre, R. J., Fields, R. D. & Johansen-Berg, H. Plasticity in gray and white: Neuroimaging
503   changes in brain structure during learning. *Nat. Neurosci.* **15**, 528–536 (2012).

504   14.   Gibson, E. M. *et al.* Neuronal activity promotes oligodendrogenesis and adaptive myelination
505   in the mammalian brain. *Science (80-.).* **344**, (2014).

506   15.   Hughes, E. G., Orthmann-Murphy, J. L., Langseth, A. J. & Bergles, D. E. Myelin remodeling

through experience-dependent oligodendrogenesis in the adult somatosensory cortex. *Nat. Neurosci.* **21**, 696–706 (2018).

16. Makinodan, M., Rosen, K. M., Ito, S. & Corfas, G. A critical period for social experience-dependent oligodendrocyte maturation and myelination. *Science (80-.).* **337**, 1357–1360 (2012).

17. Stüber, C. *et al.* Myelin and iron concentration in the human brain: A quantitative study of MRI contrast. *Neuroimage* **93**, 95–106 (2014).

18. Knickmeyer, R. C. *et al.* A structural MRI study of human brain development from birth to 2 years. *J. Neurosci.* **28**, 12176–12182 (2008).

19. Ouyang, M., Dubois, J., Yu, Q., Mukherjee, P. & Huang, H. Delineation of early brain development from fetuses to infants with diffusion MRI and beyond. *NeuroImage* **185**, 836–850 (2019).

20. Shi, F. *et al.* Infant Brain Atlases from Neonates to 1- and 2-Year-Olds. *PLoS One* **6**, e18746 (2011).

21. Wakana, S. *et al.* Reproducibility of quantitative tractography methods applied to cerebral white matter. *Neuroimage* **36**, 630–644 (2007).

22. Weiner, K. S., Yeatman, J. D. & Wandell, B. A. The posterior arcuate fasciculus and the vertical occipital fasciculus. *Cortex* (2016). doi:10.1016/j.cortex.2016.03.012

23. Takemura, H. *et al.* A Major Human White Matter Pathway Between Dorsal and Ventral Visual Cortex. *Cereb. Cortex* **26**, 2205–2214 (2016).

24. Yeatman, J. D. *et al.* The vertical occipital fasciculus: A century of controversy resolved by in vivo measurements. *Proc. Natl. Acad. Sci.* **111**, E5214–E5223 (2014).

25. Wang, Y. *et al.* Rethinking the role of the middle longitudinal fascicle in language and auditory pathways. *Cereb. Cortex* **23**, 2347–2356 (2013).

26. Yeatman, J. D., Dougherty, R. F., Myall, N. J., Wandell, B. A. & Feldman, H. M. Tract Profiles of White Matter Properties: Automating Fiber-Tract Quantification. *PLoS One* **7**, (2012).

27. Jiang, H. *et al.* Early diagnosis of spastic cerebral palsy in infants with periventricular white matter injury using diffusion tensor imaging. *Am. J. Neuroradiol.* **40**, 162–168 (2019).

28. Langer, N. *et al.* White Matter Alterations in Infants at Risk for Developmental Dyslexia. *Cereb. Cortex* **27**, 1027–1036 (2017).

29. Travis, K. E., Adams, J. N., Ben-Shachar, M. & Feldman, H. M. Decreased and increased anisotropy along major cerebral white matter tracts in preterm children and adolescents. *PLoS One* **10**, e0142860 (2015).

30. Yu, Q. *et al.* Differential White Matter Maturation from Birth to 8 Years of Age. *Cereb. Cortex* **30**, 2673–2689 (2020).

31. Partridge, S. C. *et al.* Diffusion tensor imaging: Serial quantitation of white matter tract maturity in premature newborns. *Neuroimage* **22**, 1302–1314 (2004).

32. Sadeghi, N. *et al.* Regional characterization of longitudinal DT-MRI to study white matter maturation of the early developing brain. *Neuroimage* **68**, 236–247 (2013).

33. Oishi, K. *et al.* Multi-contrast human neonatal brain atlas: Application to normal neonate development analysis. *Neuroimage* **56**, 8–20 (2011).

34. Dubois, J. *et al.* MRI of the Neonatal Brain: A Review of Methodological Challenges and

23

549   Neuroscientific Advances. *Journal of Magnetic Resonance Imaging* jmri.27192 (2020).
550   doi:10.1002/jmri.27192

551   35.   Schneider, J. *et al.* Evolution of T1 relaxation, ADC, and fractional anisotropy during early
552   brain maturation: A serial imaging study on preterm infants. *Am. J. Neuroradiol.* **37**, 155–162
553   (2016).

554   36.   Yeatman, J. D., Wandell, B. A. & Mezer, A. A. Lifespan maturation and degeneration of
555   human brain white matter. *Nat. Commun.* **5**, 4932 (2014).

556   37.   Grotheer, M., Zhen, Z., Lerma-Usabiaga, G. & Grill-Spector, K. Separate lanes for adding
557   and reading in the white matter highways of the human brain. *Nat. Commun.* **10**, 420216
558   (2019).

559   38.   Howell, B. R. *et al.* The UNC/UMN Baby Connectome Project (BCP): An overview of the
560   study design and protocol development. *NeuroImage* **185**, 891–905 (2019).

561   39.   O'Muircheartaigh, J. *et al.* Modelling brain development to detect white matter injury in term
562   and preterm born neonates. *Brain* **143**, 467–479 (2020).

563   40.   Dubner, S. E., Rose, J., Bruckert, L., Feldman, H. M. & Travis, K. E. Neonatal white matter
564   tract microstructure and 2-year language outcomes after preterm birth. *NeuroImage Clin.* **28**,
565   102446 (2020).

566   41.   Parikh, N. A., Hershey, A. & Altaye, M. Early Detection of Cerebral Palsy Using
567   Sensorimotor Tract Biomarkers in Very Preterm Infants. *Pediatr. Neurol.* **98**, 53–60 (2019).

568   42.   Ghazi Sherbaf, F., Aarabi, M. H., Hosein Yazdi, M. & Haghshomar, M. White matter
569   microstructure in fetal alcohol spectrum disorders: A systematic review of diffusion tensor
570   imaging studies. *Human Brain Mapping* **40**, 1017–1036 (2019).

571   43.   Herskind, A., Greisen, G. & Nielsen, J. B. Early identification and intervention in cerebral
572   palsy. *Dev. Med. Child Neurol.* **57**, 29–36 (2015).

573   44.   Rosenke, M. *et al.* Myelin contributes to microstructural growth in human sensory cortex
574   during early infancy. *bioRxiv* 2021.03.16.435703 (2021). doi:10.1101/2021.03.16.435703

575   45.   Smith, R. E., Tournier, J. D., Calamante, F. & Connelly, A. Anatomically-constrained
576   tractography: Improved diffusion MRI streamlines tractography through effective use of
577   anatomical information. *Neuroimage* **62**, 1924–1938 (2012).

578   46.   Zöllei, L., Iglesias, J. E., Ou, Y., Grant, P. E. & Fischl, B. Infant FreeSurfer: An automated
579   segmentation and surface extraction pipeline for T1-weighted neuroimaging data of infants
580   0–2 years. *Neuroimage* **218**, 116946 (2020).

581   47.   Li, G. *et al.* Construction of 4D high-definition cortical surface atlases of infants: Methods
582   and applications. *Med. Image Anal.* **25**, 22–36 (2015).

583   48.   Li, G. *et al.* Measuring the dynamic longitudinal cortex development in infants by
584   reconstruction of temporally consistent cortical surfaces. *Neuroimage* **90**, 266–279 (2014).

585   49.   Wang, L. *et al.* Volume-based analysis of 6-month-old infant brain MRI for autism biomarker
586   identification and early diagnosis. in *Lecture Notes in Computer Science (including subseries Lecture
587   Notes in Artificial Intelligence and Lecture Notes in Bioinformatics)* **11072 LNCS**, 411–419 (Springer
588   Verlag, 2018).

589   50.   Wu H, Dougherty RF, Kerr AB, Zhu K, Middione MJ, M. A. Fast T1 mapping using slice-
590   shuffled Simultaneous Multi-Slice inversion recovery EPI. *21st Annu. Meet. Organ. Hum. Brain
591   Mapp.* (2015).

592 51. Moré, J. J. The Levenberg-Marquardt algorithm: Implementation and theory. in 105–116
593   (Springer, Berlin, Heidelberg, 1978). doi:10.1007/bfb0067700

594 52. Pietsch, M. *et al.* A framework for multi-component analysis of diffusion MRI data over the
595   neonatal period. *Neuroimage* **186**, 321–337 (2019).

596 53. Bastiani, M. *et al.* Automated processing pipeline for neonatal diffusion MRI in the
597   developing Human Connectome Project. *Neuroimage* **185**, 750–763 (2019).

598 54. Tournier, J. D. *et al.* MRtrix3: A fast, flexible and open software framework for medical image
599   processing and visualisation. *NeuroImage* **202**, 116137 (2019).

600 55. Tournier, J. D., Calamante, F. & Connelly, A. MRtrix: Diffusion tractography in crossing
601   fiber regions. *Int. J. Imaging Syst. Technol.* **22**, 53–66 (2012).

602 56. Veraart, J. *et al.* Denoising of diffusion MRI using random matrix theory. *Neuroimage* **142**,
603   394–406 (2016).

604 57. Andersson, J. L. R., Graham, M. S., Zsoldos, E. & Sotiropoulos, S. N. Incorporating outlier
605   detection and replacement into a non-parametric framework for movement and distortion
606   correction of diffusion MR images. *Neuroimage* **141**, 556–572 (2016).

607 58. Tustison, N. J. *et al.* N4ITK: Improved N3 bias correction. *IEEE Trans. Med. Imaging* **29**,
608   1310–1320 (2010).

609 59. Dhollander, T., Raffelt, D. & Connelly, A. Unsupervised 3-tissue response function
610   estimation from single-shell or multi-shell diffusion MR data without a co-registered T1
611   image. in *ISMRM Workshop on Breaking the Barriers of Diffusion MRI* 5 (2016).

612 60. Jeurissen, B., Tournier, J. D., Dhollander, T., Connelly, A. & Sijbers, J. Multi-tissue
613   constrained spherical deconvolution for improved analysis of multi-shell diffusion MRI data.
614   *Neuroimage* **103**, 411–426 (2014).

615 61. Dice, L. R. Measures of the Amount of Ecologic Association Between Species. *Ecology* **26**,
616   297–302 (1945).

617 62. Kruper, J. *et al.* Evaluating the reliability of human brain white matter tractometry. *bioRxiv*
618   2021.02.24.432740 (2021). doi:10.1101/2021.02.24.432740

619

620